equilibrium with metallic Fe; therefore, it appears unlikely that the present-day lower mantle could be in equilibrium with metallic Fe.

REFERENCES AND NOTES

1. T. Katsura, B. Iwasaki, S. Kimura, S. Akimoto, *J. Chem. Phys.* **47**, 4559 (1967).
2. H. Sawamoto, E. Ohtani, M. Kumazawa, in *Proceedings of the 4th International Conference on High Pressures*, J. Osugi, Ed. (Physical Chemistry Society of Japan, Kyoto, 1974), pp. 194–201.
3. B. Simons and F. Seifert, *Carnegie Inst. Washington Yearb.* **78**, 625 (1979).
4. C. A. McCammon and L. Liu, *Phys. Chem. Miner.* **10**, 106 (1984).
5. L. Liu, *Earth Planet. Sci. Lett.* **33**, 101 (1976).
6. D. Canil, *ibid.* **106**, 64 (1991).
7. Previous experiments (*1, 4*) have demonstrated that equilibrium is achieved within this time.
8. C. A. McCammon and D. C. Price, *Phys. Chem. Miner.* **11**, 250 (1984).
9. Experiments have shown that x decreases by 0.002 from 920° to 1200°C at 4.5 GPa (*1*). Calculations have shown (*4*) that this difference does not increase significantly at higher pressure.
10. R. Boehler, *Geophys. Res. Lett.* **13**, 1153 (1986).
11. In particular, Sawamoto *et al.* (*2*) used a Pt capsule that also served as the heater; thus, the sample was buffered well above Fe-Fe_xO equilibrium.
12. I. Jackson, S. K. Khanna, A. Revcolevschi, J. Berthon, *J. Geophys. Res.* **95**, 21671 (1990).
13. R. M. Hazen, *Carnegie Inst. Washington Yearb.* **80**, 277 (1981).
14. The discrepancy could also be caused by a composition-dependent temperature effect (for example, if the thermal expansion of Fe_xO varied dramatically with x at high pressure). This possibility seems less likely, however. In my calculations, I assumed a constant thermal expansion for Fe_xO but, nevertheless, reproduced the temperature effect on the Fe-Fe_xO phase boundary observed from 775° to 1200°C up to pressures of 4.5 GPa (*1*). Also, thermal expansion of Fe_xO does not appear to vary with x at atmospheric pressure (*15*).
15. M. Hayakawa, J. B. Cohen, T. B. Reed, *J. Am. Ceram. Soc.* **55**, 160 (1972).
16. T. Yagi, T. Suzuki, S. Akimoto, *J. Geophys. Res.* **90**, 8784 (1985).
17. S. L. Webb, I. Jackson, J. D. Fitz Gerald, *Phys. Earth Planet. Inter.* **52**, 117 (1988).
18. C. A. McCammon, *J. Magn. Magn. Mater.* **104–107**, 1937 (1992).
19. R. M. Hazen and R. Jeanloz, *Rev. Geophys. Space Phys.* **22**, 37 (1984).
20. Hirsch (*21*) has calculated the effect of pressure and temperature on the Fe-Fe_xO buffer and showed that f_{O_2} is nearly insensitive to variation of input parameters with x. Because input parameters of (Fe,Mg)O are similar to those for Fe_xO, pressure and temperature should have a similar effect on the Fe-(Fe,Mg)O buffer.
21. L. M. Hirsch, *Geophys. Res. Lett.* **18**, 1309 (1991).
22. M. Kato, S. Urakawa, M. Kumazawa, paper presented at the DELP 1989 Misasa International Symposium and the Second Japan-USSR Symposium, Misasa, Japan, 17 to 22 April 1989.
23. Extrapolation beyond experimental-data conditions increases the uncertainty of this determination. Accordingly, I have restricted calculations to the maximum value only and allowed for uncertainties in input parameters.
24. The $Fe^{3+}/\Sigma Fe$ ratio decreases with increasing pressure to at least 18 GPa (Fig. 3) and, in the absence of phase transitions, this trend is unlikely to change significantly at higher pressure. The effect of temperature on the Fe-Fe_xO phase boundary is reduced with increasing pressure (*4*); this trend is also unlikely to change. The γ-ϵ phase transition in Fe would favor a larger $Fe^{3+}/\Sigma Fe$ ratio at higher pressures and lower temperatures, but the transition boundary crosses the Earth's geotherm only in the deep mantle (*10*), and the effect would be reduced in any event because of the small Fe concentration of the lower-mantle (Mg,Fe)O.
25. H. St. C. O'Neill *et al.*, in *Proceedings of IUGG Symposium U12*, E. Takahashi, R. Jeanloz, D. C. Rubie, Eds. (American Geophysical Union, Washington, DC, in press).
26. B. J. Wood and J. Nell, *Nature* **351**, 309 (1991).
27. J. Peyronneau and J. P. Poirier, *ibid.* **342**, 537 (1989); X. Li and R. Jeanloz, *J. Geophys. Res.* **95**, 21609 (1990); *ibid.* **96**, 6113 (1991).
28. I am grateful to Dr. Rubie for assistance with the multianvil experiments and to I. Jackson, D. Mao, H. O'Neill, S. Rigden, and F. Seifert for comments on the manuscript.

21 July 1992; accepted 2 November 1992

A Traveling-Wave Amplifier Model of the Cochlea

Allyn Hubbard

A two-mode model of the cochlea that uses active intermode feedback has been developed that quantitatively accounts for the motion of the basilar membrane in response to single tones and qualitatively accounts for cochlear emission phenomena. In contrast to existing single-mode models, this model amplifies the mechanical traveling wave in spatially localized cochlear regions where an approximate match occurs between the traveling-wave velocities of each of the two traveling-wave lines or modes.

The concept of a "second filter" in the mammalian cochlea was originally proposed to account for the apparent discrepancy between broadly tuned cochlear micromechanics (*1*) and highly tuned, auditory nerve responses (*2*). This concept has been abandoned in the past decade because of experiments demonstrating little difference between the tuning properties of the cochlear mechanics (*3*), the sensory receptors (*4*), and the auditory nerve fibers. This report proposes a model that matches mechanical data (*5*) extremely well and, therefore, has the potential to expand our understanding of the mechanisms underlying the unique sensitivity and frequency selectivity of the cochlea.

Cellular and extracellular structures partition the cochlea into several longitudinal, fluid-filled ducts (Fig. 1). The anatomical picture is far more complicated than classical cochlear models (*6*), which approximate the major partition between upper and lower scalae as a single membrane. The membrane was assumed to respond to the pressure difference between the scala tympani and scala vestibuli, resulting in a single vibration mode that propagates acoustic energy down the cochlea. However, in a structure like that of Fig. 1, every duct and boundary partition can support propagation modes. My model shows that we can produce realistic cochlear responses using two actively coupled modes.

The active components of this model are the cochlear outer hair cells that abut the upper and lower boundary structures in the fluid-filled outer tunnel. Depolarization of isolated outer hair cells causes a decrease in cell body length and generates forces of about 0.5 nN/mV. For voltage changes comparable to those that occur in the natural cochlear transduction process, reproduced by electrical stimulation of the cochlea, significant acoustic signals can be measured at the eardrum [see (*7*)]. Therefore, it is reasonable to believe that in vivo hair cells respond to their receptor current by changing their length, thus exerting microforces on other cochlear structures, which, in a yet unknown way, produces amplification of the mechanical traveling wave. In my model, forces are exchanged (fed back) between the transmission lines, each representing a different mode of wave propagation.

Earlier models have used local feedback (*8*), but the feedback apparatus appended to each model segment was not longitudinally connected to form an additional propagation mode. Zweig's (*9*) locally applied feedback expression was derived under the condition that the feedback cause the classical model (*6*) to fit modified experimental data. De Boer (*10*) has described possible modes in a multiple-duct model. My work demonstrates that coupling two modes with the use of feedback results in a type of traveling-wave amplifier.

Classical electronic traveling-wave amplifiers (*11*) are composed of two transmission lines connected by transistors along their lengths. The transmission lines are made up of concatenated passive components. The input signal travels along one line, providing a control signal to the transistors. The control signal causes the transistors to regulate the current supplied to the second transmission line, called the output line. The most constructive current addition occurs when the propagation velocities on both lines are equal. Thus, an ever-growing signal travels down the output

---

College of Engineering and School of Medicine, Boston University, Boston, MA 02215.

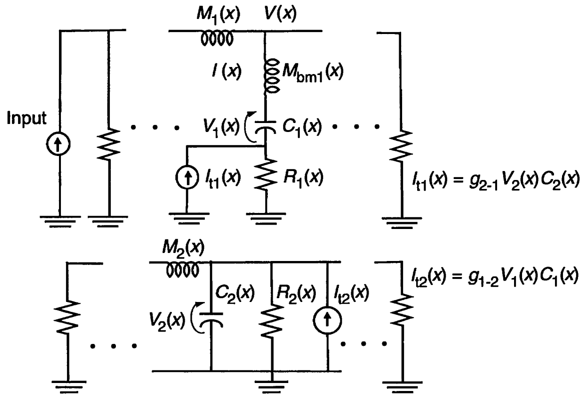

Fig. 2. One incremental segment of model. *I*, current; *V*, voltage; *M*, inductance; *C*, capacitance; *R*, resistance; *g*, gain. Connecting 400 similar sections forms two transmission lines, which are terminated at each end as shown.

line in a feed-forward, not feed-back, situation. The practical pitfall is that unavoidable losses in the input line dissipate the control signal.

My model regenerates signals on both lines over a frequency-specific region. One line is a classical, resonant, basilar membrane model. A wave traveling on that line alone moves at a high velocity up to a point near the (spatial) point of resonance, where it slows considerably over a short distance. The separate second line is not resonant. Wave velocities at any location are in the range of the first line's velocities near resonance. When the lines are coupled, the wave travels on both lines at the same velocity. Initially the velocity is like that of the (separated) resonant line with its parameters altered by feedback. Near the altered resonant location, the wave slows to approximately the velocity of the (separated) second line and remains at that velocity over a limited spatial region. Significant amplification occurs here.

I quantified the performance of the model by building an analogous electric circuit consisting of two transmission lines coupled incrementally using dependent sources (Fig. 2). When multiple segments are linked together, waves travel by exchanging energy between reactive components. The upper line represents the classical, resonant, cochlear model, whose parameters were chosen with respect to known cochlear physiology [see (*12*)]. The lower line's parameters were chosen so that its group velocity is slow relative to the basilar membrane line (except in the input-frequency–specific spatial region where resonance occurs). Coupling the two lines are dependent current sources, I_{tn}. The degree of active coupling depends on the size of the gain factors ($g_{1\text{-}2}$, $g_{2\text{-}1}$). The input to the upper line is proportional to the velocity of the stapes, the middle-ear bone that transmits sound to the cochlea.

The results have been compared with data from cat, monkey, guinea pig, and chinchilla. Chinchilla data were chosen for presentation because they show the largest peak output/input ratios which, in turn, imply the best experimental conditions. Figure 3A shows model magnitude data (*13*) and experimental data (*5*). There is agreement, specifically with the very low frequency slope, the mid-frequency relatively reduced slope, and the height and bandwidth of the peak response. If the gains are set to zero, the maximum response is significantly reduced and occurs at a lower frequency. Active model phase data (Fig. 3B) compare favorably with experimental phase data, falling generally within the extremes of phase angle for five animals. The experimentally obtained, high-frequency phase asymptote differs by about 360° in different animals. In the model, parameter variations can cause 360° variations in the phase plateau. A phase lead occurs at 6.5 kHz, coinciding with the null in magnitude response. The model's impulse response (Fig. 4) strongly resembles the experimentally determined click response (*14*).

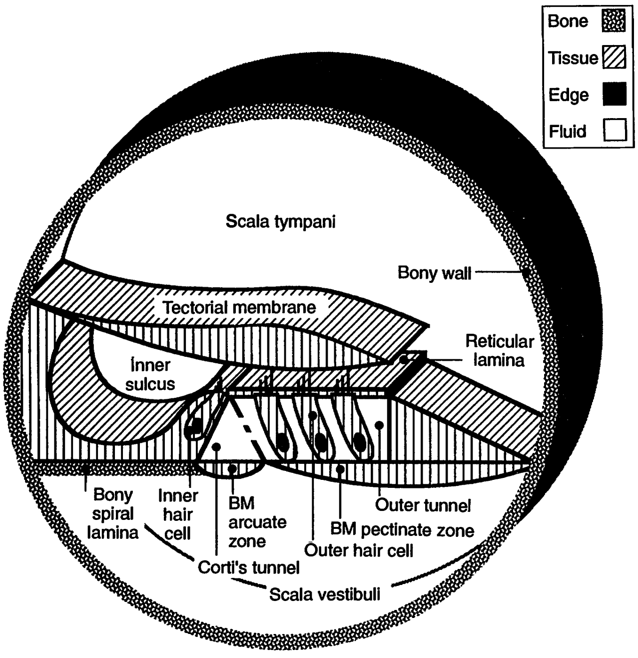

Fig. 1. Schematized cross section of a longitudinal slice of cochlea. BM, basilar membrane.

The model (qualitatively, at this stage) accounts for several types of cochlear emissions. With sufficiently high gain, the active mechanism locally increases pressure [Fig. 2, $V(x)$] in the cochlear scala at frequencies near the peak velocity response. The increase (4 dB) can be viewed from the input of the model as a stimulus-frequency emission (*15*). Click-evoked emissions occur (Fig. 4) as the result of two factors: The early response ($<$1.5 ms) is the result of after-ringing in the motion of many model sections, each of which contributes to a summed pressure response. A purposely introduced discontinuity in the gains at a single model section (*16*) causes the lower frequency "echo" (2.0 to 4.5 ms), which has a periodicity characteristic of its originating cochlear location. Physiologically occurring, click-evoked emissions (*17*) are thought to be produced by discontinuities in the cochlea. Spontaneous emissions (*18*) occur in the model when a region of simulated cochlea has sufficiently high gain.

The model differs strikingly from local-feedback models whose active single-section performance is highly tuned relative to their passive single-section performance (*19*). The velocity response of a single segment of the active model (*20*) resembles the single-segment passive response but is shifted so that its maximum occurs at the same frequency as the multisection active model. The 3-dB bandwidths of all peaks, including that of the multisection active model, are comparable (*21*). However, the active full-model peak is remarkably elevated, completely unlike the active single-section case (*22*).

The new model produces a significant (~40 dB) reduction in virtual basilar mem-

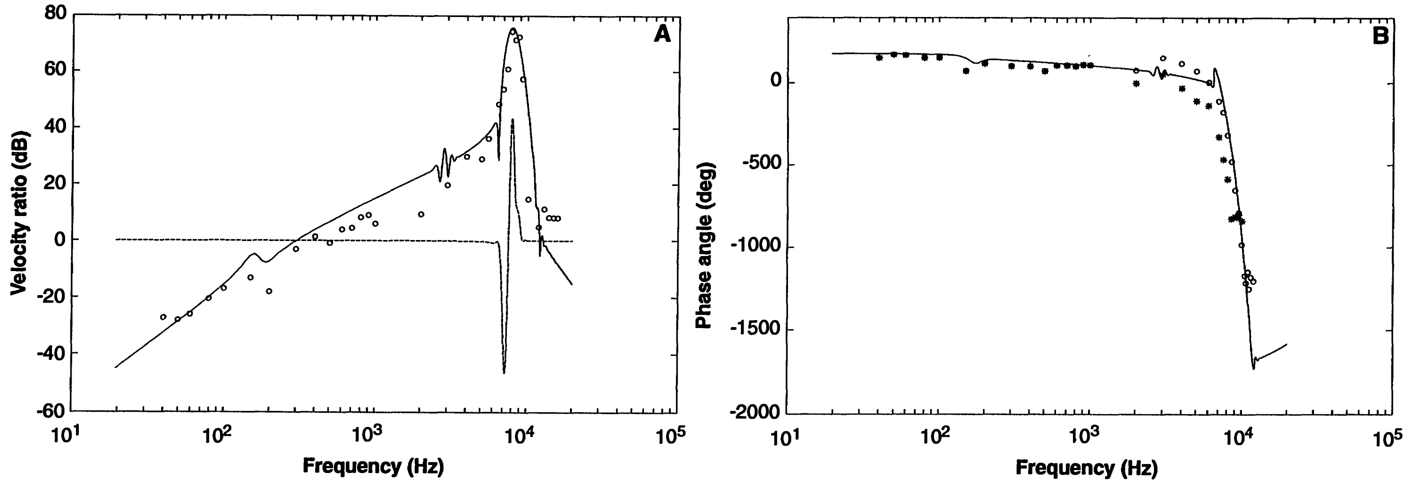

Fig. 3. Comparison of model data (*13*) (solid lines) and experimental data (*5*) from the chinchilla (points). (**A**) The ratio of basilar membrane to stapes velocity. Calculated power (dashed line) is on an arbitrary linear *y*-axis (peak power is 0.032 cgs acoustic picowatts for input corresponding to 0-dB sound pressure level). (**B**) Phase angle of responses relative to stapes velocity. The points * and O are the extremes of experimental data.

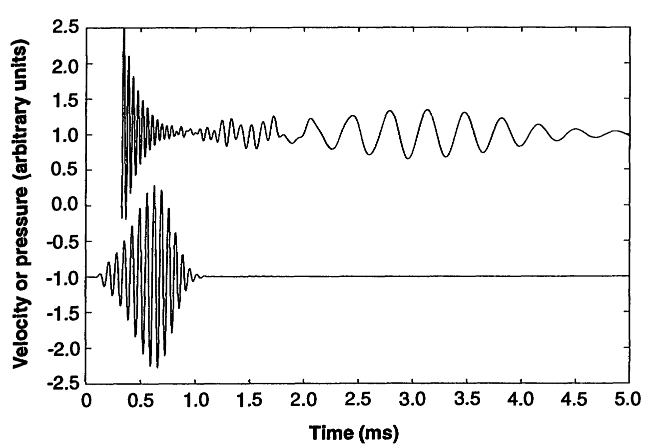

Fig. 4. Two types of impulse responses from model. Lower trace: velocity response (*13*); upper trace: pressure response at input. Initial data are zeroed in order to concentrate on the "echoes." The peak reflected signal was 1/150th of the peak input pressure.

brane impedance (*10, 23*) near peak response frequencies. The small impedance alternates, having positive and negative, real and imaginary parts. The active impedance at cochlear locations toward the input from a tuned location is a relatively stiffer-than-passive spring and a negative damping, as predicted theoretically (*24*) to occur in the cochlea. However, over those regions the overall impedance is high. Consequently, salient power generation (Fig. 3A) by the basilar membrane (*23*) can be restricted to the maximum response region. This contrasts with conventional speculation and published results from existing models in which significant power is produced in a broad region well before the tuned peak. Recently published experimental data are clearly at odds with that concept and instead support the present model (*25*).

The model's amplification mechanism is robust. The velocity on the resonant line, separately excited (*22, 26*), might drop an order of magnitude, assuming physiologically reasonable damping factors. Therefore, a second-mode velocity need only be set within this order of magnitude for some amplification to occur (*27*). Given constant mass, for example, stiffness could vary by ~×100 because velocity goes as the square root. Therefore, this model is a good candidate for a parameter-tolerant, biological amplifier.

The model poses a challenge for the future to confirm the existence of physiologically significant modes and to locate anatomical correlates. The first mode likely corresponds to the pectinate region of the basilar membrane. There are several anatomical candidates for the second transmission line, which may be interpreted as either an acoustic or a mechanical analog (*12*). Additionally, either or both transmission lines may represent dominant modes of a more complicated, multiduct model.

REFERENCES AND NOTES

1. G. von Bekesey, *Phys. Z.* **29**, 793 (1928).
2. N. Kiang, T. Watanabe, E. Thomas, L. Clark, *Discharge Patterns of Single Fibers in the Cat's Auditory Nerve* (MIT Press, Cambridge, MA, 1965).
3. W. Rhode, *J. Acoust. Soc. Am.* **49**, 1218 (1971); P. Sellick, R. Patuzzi, B. Johnstone, *ibid.* **72**, 131 (1982); S. M. Khanna and D. G. B. Leonard, *Science* **215**, 305 (1982); L. Robles, M. Ruggero, N. Rich, *J. Acoust. Soc. Am.* **80**, 1364 (1986).
4. I. Russell and P. Sellick, *J. Physiol.* (*London*) **284**, 261 (1986).
5. M. Ruggero, N. Rich, L. Robles, B. Shivapuja, *J. Acoust. Soc. Am.* **87**, 1612 (1990).
6. L. Peterson and B. Bogert, *ibid.* **22**, 369 (1950).
7. W. E. Brownell, C. R. Bader, D. Bertrand, Y. de Ribaupierre, *Science* **227**, 194 (1985); K. Iwasa and R. Chadwick, *J. Acoust. Soc. Am.* **92**, 3169 (1992); A. E. Hubbard and D. C. Mountain, *Science* **222**, 510 (1983).
8. E. Zwicker, *Biol. Cybern.* **35**, 243 (1979).
9. G. Zweig, *J. Acoust. Soc. Am.* **89**, 1229 (1991).
10. E. de Boer, in *The Mechanics and Biophysics of Hearing*, P. Dallas *et al.*, Eds. (Springer-Verlag, New York, 1990), pp. 333–339.
11. E. Ginzton, W. Hewlett, J. Jasberg, J. Noe, *Proc. IRE* **36**, 956 (1948); Y. Ayasli, L. Reynolds, R. Mossi, L. Hanes, *IEEE Trans. Microwave Theory Tech.* *MTT* **32/33**, 290 (1984).
12. The electrical variables and parameters of the upper line are acoustic analogs of the impedance type. Voltage corresponds to pressure and current to volume velocity. Scala cross-sectional area implies the acoustic mass, $M_1(x)$. A group velocity profile (100 m/s at the base, decreasing exponentially to 0.1 m/s at apex) determines compliance, $C_1(x)$. An approximation to the experimentally determined best frequency (20 kHz base to 200 Hz apex) versus location map determines the acoustic mass, $M_{1bm}(x)$, based on resonance. The Q of each section is 4. The shunting resistance, $R_2(x)$, is equal to the approximate characteristic impedance seen at that point. Cs are equal at section 170. $M_2(x)$ is $2M_1$ exp$(4j/400)$, $0 < j < 401$. The lines are terminated at each end in their approximate characteristic impedance. The gains are -3×10^5 and -2×10^5, each reduced linearly by 90% from base to apex. The same parameters are used for all results shown. Volume velocities (basilar membrane/stapes) were (64 dB is the factor) translated to linear velocities for comparison with data recorded in anatomical dimensions. The simulation was done with CAzM, a simulator produced by the Microelectronics Center of North Carolina. Experimentation with tolerance factors and numbers of sections was done so that I could be convinced of the simulation program's accuracy. No feature in the results presented is an artifact. Simulations were carried out with the parameters given above and scaled by 10^5, which yielded scaled but identical results.
13. Output is from model section 99, which is 3.25 mm from the stapes.
14. M. Ruggero and N. Rich, *Hear. Res.* **51**, 215 (1991).
15. J. Guinan, in *The Mechanics and Biophysics of Hearing*, P. Dallas *et al.*, Eds. (Springer-Verlag,

New York, 1990), pp. 170–177.
16. At model section 200, the algorithmically calculated gain of the dependent source feeding into the upper line was manually assigned the same value as section 199. This was about a 5.8% variation from the originally assigned gain for that section.
17. D. Kemp, *J. Acoust. Soc. Am.* **64**, 1386 (1978).
18. J. Wilson, *Hear. Res.* **2**, 233 (1980).
19. D. Shine, thesis, Boston University (1991).
20. I removed section 99 and used a voltage source to drive it. Longitudinal inductors were not present.
21. The single-section active 3-dB bandwidth is ≈2000 Hz, about twice that of every other 3-dB bandwidth.
22. I confirmed the hypothesized velocity match region by running the model with $M_2(x) = \infty$ in the lower line and comparing phase-versus-frequency results (*26*) for this configuration and for the lower line disconnected from the upper line. The full model in the local-feedback configuration produces passive-looking, not elevated, peaks on the upper line. This behavior also demonstrates the distributed nature of the amplification.
23. Impedance is $V(x)/I(x)$. Power is $V(x)I(x)$. See Fig. 2.
24. E. de Boer, *J. Acoust. Soc. Am.* **73**, 567 (1983).
25. A. Cody, *Hear. Res.* **62**, 166 (1992); A. Hubbard, D. Gonzales, D. Mountain, Abstracts of the 16th Midwinter Meeting of the Association for Research in Otolaryngology, accepted for publication. See also J. Allen and P. Fahey [*J. Acoust. Soc. Am.* **92**, 178 (1992)], who uses experimental data to show there is little or no cochlear amplification.
26. Group delay is (minus) the slope of the phase-versus-frequency curve.
27. One must more carefully chose parameters to match specific data.
28. A. Cody, D. Gonzales, P. Jung, D. Mountain, H. Voigt, and S. Xue aided the preparation of this manuscript. Support provided by the Office of Naval Research and NIH.

26 May 1992; accepted 7 October 1992

Vapor Pressures of Solid Hydrates of Nitric Acid: Implications for Polar Stratospheric Clouds

Douglas R. Worsnop,* Lewis E. Fox, Mark S. Zahniser, Steven C. Wofsy

Thermodynamic data are presented for hydrates of nitric acid: $HNO_3 \cdot H_2O$, $HNO_3 \cdot 2H_2O$, $HNO_3 \cdot 3H_2O$, and a higher hydrate. Laboratory data indicate that nucleation and persistence of metastable $HNO_3 \cdot 2H_2O$ may be favored in polar stratospheric clouds over the slightly more stable $HNO_3 \cdot 3H_2O$. Atmospheric observations indicate that some polar stratospheric clouds may be composed of $HNO_3 \cdot 2H_2O$ and $HNO_3 \cdot 3H_2O$. Vapor transfer from $HNO_3 \cdot 2H_2O$ to $HNO_3 \cdot 3H_2O$ could be a key step in the sedimentation of HNO_3, which plays an important role in the depletion of polar ozone.

Polar stratospheric clouds (PSCs) (*1–3*) play two essential roles in perturbing the chemistry of stratospheric O_3 during winter: (i) PSCs provide reactive surfaces that convert inorganic chlorine to reactive form and nitrogen oxides to HNO_3 (*4, 5*) and (ii) sedimentation of PSC particles containing HNO_3 leads to irreversible removal of nitrogen oxides ("denitrification"). The efficiency of denitrification is crucial for polar O_3 depletion. If substantial gaseous HNO_3 is present in late winter, it photolyzes to release NO_x radicals, which combine with ClO, halting O_3 destruction (*4, 6*). Denitrification is nearly complete over Antarctica and large O_3 losses are observed (*7*); denitrification is sporadic in the Arctic (*8*) and O_3 losses are much smaller.

Type I PSCs condense at temperatures 2 to 4 K above the frost point of water ice (*1*). Solid hydrates of HNO_3 have been proposed as the major components of type I PSCs (*2, 3*), and nitrogen oxides have been observed in PSC particles (*7, 8*). The principal phase is usually assumed to be nitric acid trihydrate ($HNO_3 \cdot 3H_2O$) (*2, 3, 6*), the most stable hydrate under stratospheric conditions (*9*). However, careful analysis of field observations of total nitrogen oxides and aerosol particles (*10*) indicates that PSCs form at temperatures 2 to 4 K colder than the equilibrium temperature for $HNO_3 \cdot 3H_2O$. Partial pressures of HNO_3 in PSCs (*11*) were observed to exceed equilibrium with $HNO_3 \cdot 3H_2O$; this led Arnold (*12*) to argue that the condensed phase could be a supercooled liquid (*13*) rather than $HNO_3 \cdot 3H_2O$.

This report presents the results of laboratory studies of hydrates of HNO_3 under conditions of temperature and gas-phase HNO_3 and H_2O concentrations approaching those found in the stratosphere. We show that nitric acid dihydrate ($HNO_3 \cdot 2H_2O$) is only slightly less stable than $HNO_3 \cdot 3H_2O$ and is a likely metastable component of type I PSCs. Thin films of $HNO_3 \cdot 2H_2O$ have been reported (*14*), but no thermodynamic information has been available. We also identify a higher hydrate, possibly $HNO_3 \cdot 10H_2O$ (*15, 16*).

Vapor pressures of HNO_3 and H_2O were measured by infrared tunable diode laser absorption spectroscopy with a multiple-pass Herriott cell (40 passes, 50 cm per pass; 7.6-cm-diameter gold-coated mirrors) mounted vertically in a 12-liter vacuum chamber constructed of gold-plated stainless steel and glass coated with $C_6F_{13}CH_2CH_2Si(OC_2H_5)_3$ (Petrarch Systems) (see Fig. 1). We determined partial pressures p_{H_2O} and p_{HNO_3} by fitting Gaussian line profiles for 12 HNO_3 lines and 1 H_2O line between 1339.97 and 1340.18 cm^{-1}, with line strengths derived from recent measurements (*17*). Detection limits were $\sim 10^{-7}$ torr for HNO_3 and $[HNO_3]/50$ for H_2O, limited by interference fringes for HNO_3 and by a weak HNO_3 feature for H_2O.

We regulated sample temperatures between 190 and 230 K by allowing cold nitrogen gas to flow onto a brass button epoxied to the cell exterior 20 cm below the detection region. We condensed solid phases on the glass surface above the button by cooling mixtures of gaseous H_2O and HNO_3 or by adding gaseous H_2O or HNO_3 to a cold sample. The thickness of the condensed layer varied between 5 and 50 µm, estimated from the amount of gas-phase H_2O and HNO_3 that condensed. The button temperature could be regulated with a precision of ±0.2 K [accuracy approximately ±0.4 K (*18*)], as confirmed by comparing p_{H_2O} to literature values (*19*). The cell temperature above the cold point was set to 273 K for most experiments. Heating or cooling the Herriott cell between 240 and 295 K had no measurable effect on vapor pressures, indicating negligible influence of gases adsorbed on chamber walls.

The chamber was sealed under vacuum during the experiments, except during the addition of H_2O or HNO_3 through the manifold. Mixtures placed into the cell typically did not match the stoichiometry of a crystalline hydrate; consequently, two or three solid phases condensed on the cold spot in equilibrium with a vapor phase ("triple" or "quadruple" points, respectively). Partial pressures (p_{HNO_3} and p_{H_2O}) equilibrated with a surface layer of a single crystalline phase when vapor was added to the chamber. For example, in an experiment in which $HNO_3 \cdot 3H_2O$ and ice were condensed above the cold button, a surface layer of $HNO_3 \cdot 3H_2O$ alone was formed on addition of HNO_3 at pressures of 10^{-4} to 2×10^{-2} torr. Vapor pressures in the cell equilibrated with this layer, as demonstrated by the variation of p_{HNO_3} and p_{H_2O} according to the Gibbs-Duhem equation

$$d(\ln p_{HNO_3})/d(\ln p_{H_2O}) = -n \quad (1)$$

where n is the H_2O/HNO_3 ratio in the solid phase. Over a period of many minutes, water diffused from the underlying solid, driving p_{HNO_3} and p_{H_2O} back to the triple point according to Eq. 1 (with $n = 3$). This behav-

---

D. R. Worsnop and M. S. Zahniser, Center for Chemical and Environmental Physics, Aerodyne Research, Inc., Billerica, MA 01821.
L. E. Fox and S. C. Wofsy, Division of Applied Sciences, Harvard University, Cambridge, MA 02138.

*To whom correspondence should be addressed.